Nanoscale

ROYAL SOCIETY OF CHEMISTRY

PAPER

View Article Online
View Journal | View Issue

Cite this: *Nanoscale*, 2022, **14**, 17976

In situ generated Cu–Co–Zn trimetallic sulfide nanoflowers on copper foam: a highly efficient OER electrocatalyst†

Jie Bai, Nana Lei, Limin Wang* and Yaqiong Gong *

The electrocatalytic oxygen evolution reaction (OER) is an integral part and a stepping stone to various electrochemical technologies in the field of electrochemical energy conversion. The development of OER catalysts with low-cost materials, industry-related activity and long-term durability is highly needed, but remains challenging at this stage. In this paper, Cu ions in a copper foam (CF) substrate were replaced with $Cu(OH)_2$ grown on CF to participate in the subsequent reaction, and then a subsequent two-step hydrothermal method was used to obtain the nanoflower-like Cu–Co–Zn trimetallic sulfide (named CuCoZn–S-3) catalyst, whose unique flower structure ensures that the catalyst surface exhibits a larger electrochemical active area, so as to expose plentiful active sites. The synergism between metals regulates the electron environment and accelerates the charge transfer rate, greatly improving the electrocatalytic activity of the catalyst. The prepared CuCoZn–S-3 exhibits excellent OER performance under alkaline conditions. It requires overpotentials of only 175 mV and 242 mV to drive current densities of 10 mA cm^{-2} and 100 mA cm^{-2}, respectively. The Tafel slope of CuCoZn–S-3 is 62.3 mV dec^{-1}. This study may provide a viable strategy for the rational preparation of low-cost and efficient OER electrocatalysts in alkaline medium.

Received 8th August 2022,
Accepted 31st October 2022

DOI: 10.1039/d2nr04335a

rsc.li/nanoscale

1. Introduction

With the energy crisis and environmental pollution, the development and utilization of hydrogen energy has been deemed as one of the important ways to cope with global climate change, ensure national energy security and realize low-carbon transformation.[1,2] Hydrogen energy, as a clean, efficient and sustainable energy source, has been widely used in large-scale industries such as ammonia synthesis and hydrogenation in smelters.[3] Electrochemical water splitting is the most potential large-scale application of green hydrogen production technology due to its low cost, convenient operation and no pollution nature.[4,5] In general, water splitting can be divided into hydrogen evolution reaction (HER) and oxygen evolution reaction (OER), and under alkaline conditions, the OER can be interpreted as $4OH^- \rightarrow 2H_2O + 4e^- + O_2$, which is a sluggish four electron transfer process and recognized as the decisive step of water splitting.[6,7] Generally, the commonly used OER catalysts are mainly precious metals and their oxides, such as RuO_2 or IrO_2, which can significantly reduce overpotential and immensely increase response rates. However, limited reserves and high cost seriously hampered their wide range of industrial practical applications.[8] Hence, it is imperative to develop non-noble metal based OER electrocatalysts with abundant resources, low price, stable activity and excellent catalytic performance.

In recent years, transition metal oxides,[9,10] phosphates,[11,12] sulfides,[13,14] nitrides[15,16] and layered hydroxides (LDHs)[17–19] have been extensively developed as transition metal based catalysts. Among them, sulfides are considered as viable electrocatalysts because of their advantages of low cost, high electrical conductivity and convenient synthesis.[20,21] Moreover, many bimetallic sulfides have been reported to enhance OER catalytic activity due to synergistic effects and richer redox active sites compared to mono-metallic sulphides.[22] Manivelan *et al.* propounded copper sulfide-coupled cobalt sulfide nanosheets as an electrocatalyst and a lower overpotential of 240 mV was required to drive current densities of 10 mA cm^{-2} for the OER.[23] Zhang *et al.* fabricated the heterostructure nanowire catalyst Ni_3S_2-Co_9S_8 by a two-step hydrothermal method, and only an overpotential of 294 mV was needed to reach a current density of 20 mA cm^{-2}.[24] Chinnadurai *et al.* synthesized a bimetallic CuNiS electrocatalyst using a one-step chemical bath deposition (CBD) method, and found that when the current density approached 10 mA cm^{-2}, the overpotential was only 337 mV.[25] The above experimental reports indicate that the essence of the improved catalytic performance of a bimetallic

School of Chemical Engineering and Technology, North University of China, Taiyuan, 030051, China. E-mail: wanglimin@nuc.edu.cn, gyq@nuc.edu.cn

† Electronic supplementary information (ESI) available. See DOI: https://doi.org/10.1039/d2nr04335a

sulfide system is the charge transfer between the two metal elements,[26,27] which may regulate the electronic configuration around metal element sites to obtain appropriate binding energies with intermediates *O or *OOH.[28–30] In addition, it has been reported that compared with bimetallic sulfides, trimetallic sulfides can better regulate the electronic structure and metal synergistic effect in the OER, and promote the reaction kinetics.[31,32] Therefore, we believe that the introduction of transition metal elements to prepare trimetallic sulfides can be considered an available strategy to further improve the OER performance of the catalyst.[33,34]

In addition, changing the catalyst structure or regulating the morphology of the catalyst exerts a certain impact on the performance. Morphological and structural changes can increase the number of active sites on the functional interface, improve the physical properties of the catalyst, and thus accelerate the electrocatalytic performance of the catalyst.[35–37] Simple transition metal sulfides have the disadvantages of easy self-agglomeration, low intrinsic conductivity and insufficient active sites, which have a certain influence on the morphology and properties of the catalyst. Combining transition metal sulfides with conductive substrates is considered to control the structure and morphology of the catalyst, enhance the electronic conductivity of the material, and increase the number of active sites on the surface, so as to improve the electrochemical performance of the prepared catalyst.

In this paper, a nanoflower-like catalyst CuCoZn–S-3 on CF was proposed by one-step pretreatment and a two-step hydrothermal method and thus applied as an efficient OER electrocatalyst. The flower structure can provide a tremendous specific surface area, expose abundant active sites, make surfactants participate in a redox reaction, and further accelerate charge transfer. At the same time, the formation of a flower structure will also provide the catalyst surface with a large gap, so that the electrolyte and the catalyst completely come into contact at the interface, accelerating the gas release process of the oxygen evolution reaction. In addition, the different valence states and synergies between Cu, Co and Zn availably enrich the redox reaction and significantly improve the electrochemical performance. When the current density was 10 mA cm^{-2} and 100 mA cm^{-2}, the OER overpotentials needed were only 178 mV and 242 mV, and the OER maintained favorable structural stability and catalytic activity in a 20 h stability test.

2. Experimental

2.1 Materials

CF was provided by Suzhou Taili Foam Metal Co., Ltd. Sodium hydroxide (NaOH, 99%) and cobalt nitrate hexahydrate ($Co(NO_3)_2{\cdot}6H_2O$, 99%) were bought from Beijing Innochem Technology Co., Ltd. Zinc nitrate ($Zn(NO_3)_2{\cdot}6H_2O$, 99%) was purchased from Tianjin Guangfu Technology Development Co., Ltd. Commercial Ir/C (20%) was bought from Adamas Chemical Reagent Co., Ltd. Ammonium persulfate ($(NH_4)_2S_2O_8$, 99%) and urea ($CO(NH_2)_2$, 99%) were bought from Shanghai Aladdin Biochemical Technology Co., Ltd. Ammonium fluoride (NH_4F, 98%) was bought from Shanghai Nine-Dinn Chemistry Co., Ltd. Sodium sulfide nonahydrate ($Na_2S{\cdot}9H_2O$, 98%) was obtained from Shanghai Macklin Biochemical Co., Ltd. The above chemical reagents were of analytical grade and were not further purified when used.

2.2 Synthesis of $Cu(OH)_2$

To the prepared 1 M HCl, separated CF with a size of 1 cm × 2 cm was added. In order to remove surface impurities and oxide layers, it was subjected to ultrasound and reacted for 10 min. Then the removed copper foam was soaked in a 30 mL mixture (acetone : isopropanol : water = 1 : 1 : 1) for 30 min. The processed CF was used for the next step; in 30 mL of deionized water, 2.5 M NaOH and 0.125 M $(NH_4)_2S_2O_8$ were added, and then the treated CF is placed in it; the solution turned from colorless to blue, indicating the growth of $Cu(OH)_2$ on CF; it is removed after 40 min and rinsed with deionized water and acetone.

2.3 Synthesis of CuCoZn–OH

A mixture of 1 mmol $Co(NO_3)_2$ and 0.5 mmol $Zn(NO_3)_2$ was dissolved in 20 mL of deionized water; then 5 mmol urea and 2 mmol NH_4F were added. After ultrasonic dissolution, the solution was transferred to a 50 mL Teflon-lined autoclave and put into a piece of prepared $Cu(OH)_2$. The reaction was carried out in an oven for 6 h at 120 °C. After the reaction was complete and the mixture cooled down, the samples were washed with deionized water and dried in air for 3 h.

2.4 Synthesis of CuCoZn–S-*X*

A piece of the precursors obtained above was placed and the prepared 0.1 mol L^{-1} Na_2S aqueous solution was transferred to a 50 mL Teflon-lined autoclave, reacted in an oven at 120 °C for 1 h, 3 h, and 6 h, and dried at 60 °C for 3 h. The products of the three reactions were denoted as CuCoZn–S-*X* (*X* = 1, 3, 6).

2.5 Synthesis of Ir/C on CF

10 mg of iridium carbon was dissolved in 950 μL of ethanol and 50 μL of Nafion solution was dissolved in 1 mL of the mixture with ultrasound for 30 min to obtain a uniform suspension. 100 μL of mixture was measured and four drops were added onto an area of 0.5 cm^2 CF and allowed to dry at room temperature.

2.6 Materials characterization

Scanning electron microscopy (SEM, TESCAN MIRA LMS) was used to observe the nano-structure and morphology of the samples. The morphology and structure of the synthesized samples were characterized by TEM (JEM 2100F) and the mapping distribution of elements. Inductively coupled plasma-optical emission spectrometry (ICP-OES) measurements were carried out on an Agilent 5110. The chemical composition and crystal structure of the catalyst were determined by X-ray diffraction (XRD, PANalytical Empyrean) and the

surface valence of the sample was characterized by X-ray photoelectron spectroscopy (XPS, Thermo Scientific K-Alpha).

2.7 Electrochemical measurements

Electrochemical tests were performed in 1 M KOH solution using a CHI 660E electrochemical workstation (CH Instruments, Inc. Shanghai). The prepared sample can be directly used as the working electrode without any treatment. The test area was 0.5 cm^2, a graphite rod was used as the counter electrode, Hg/HgO was used as the reference electrode, and then a standard three-electrode system was formed for subsequent testing. All electrochemical measurements were converted to values relative to a reversible hydrogen electrode (RHE) based on the formula: ERHE = $E_{Hg/HgO}$ + 0.059 × pH + 0.098 and the overpotential (η) was calculated using the formula: η = ERHE − 1.23 V. The OER performance was evaluated by linear sweep voltammetry (LSV), cyclic voltammetry (CV), and electrochemical impedance spectroscopy (EIS). Each electrochemical measurement was preceded by a 20-cycle CV scan at a scanning rate of 5 mV S^{-1} to activate the catalyst. The final LSV polarization curve was obtained at a scan rate of 1 mV S^{-1} and the EIS test range was between 0.1 Hz and 100 kHz. The stability was measured by chronopotentiometry.

3. Results and discussion

The catalyst preparation process is shown in Fig. 1. Firstly, we pretreated the prepared $Cu(OH)_2$ on a CF substrate to replace Cu ions in the substrate, so as to ensure sufficient concentration of Cu ions and $Cu(OH)_2$ on CF that can be used as the growth base for the material. Then Co and Zn elements were introduced by a hydrothermal method; the precursors of CuCoZn–OH assembled by acupuncture were acquired. Finally, the prepared catalyst CuCoZn–S-3 was composed of nanorods stacked into leaves and formed a 3D nanoflower-like structure using a 3 h hydrothermal sulfidation reaction. Related reaction principles and formulas are provided in the ESI.†

The morphology and microstructure of the prepared catalysts were studied by scanning electron microscopy (SEM). Fig. S1a† shows the SEM image of CF, which is a typical 3D porous structure. The further enlarged image shows the smooth surface of CF (Fig. S1b and c†). By preparing $Cu(OH)_2$, more Cu ions in CF were replaced to participate in the subsequent reaction. From the SEM images of $Cu(OH)_2$ in Fig. S1d–f,† it can be seen that nanowires grown vertically *in situ* are evenly distributed and cover the surface of CF. Then $Cu(OH)_2$ was used as the substrate to participate in the reaction, and Co and Zn were added to obtain the precursor CuCoZn–OH (Fig. 2a–c), which was composed of nanoneedles and a flaky nanoflower structure. After hydrothermal vulcanization, CuCoZn–S-3 with a stereoscopic nanoflower structure was obtained. As shown in Fig. 2d–f, the enlarged SEM image clearly shows that the original nanoneedles disappeared and transformed into relatively coarse nanorods, which formed 3D nanoflower-like structures through layer by layer assembly. Fig. 2g–i shows the flower-like structure formed by nanorods wrapped by $Cu(OH)_2$ as a substrate with only the Co source after vulcanization. Fig. 2j and k shows the uniformly distributed nanosheets obtained after $Cu(OH)_2$ was added as the substrate and only the Zn source was added. It was found that the morphology of CuCoZn–S-3 was formed by the interaction of Co and Zn ions.

In addition, by regulating the curing time, the morphology of the catalyst became slightly different. As shown in Fig. S2a and b,† when the curing time was 1 h, CuCoZn–S-1 initially formed a flower-like structure, which accumulated from rods to a single flower-like structure. When the curing time was prolonged to 6 h, the morphology of the CuCoZn–S-6 catalysts changed (Fig. S2c and d†), and the rods joined to form a large blade, which was then piled up to form a new flower-like structure. In other words, the sulfurization process will cause the accumulation of the nano-structure of the catalyst, resulting in a morphology change.

The microstructure of the catalyst can be further analyzed by transmission electron microscopy (TEM). Fig. 3a–c further show that the chemical agent is composed of nanorods stacked layer by layer into a flower-like structure. The HRTEM image (Fig. 3d) clearly shows the lattice fringes of these three components, which are spaced at 0.258 and 0.237 nm and can be indexed to the (2 9 3) and (2 4 8) planes of Cu_2S. The (2 2 2)

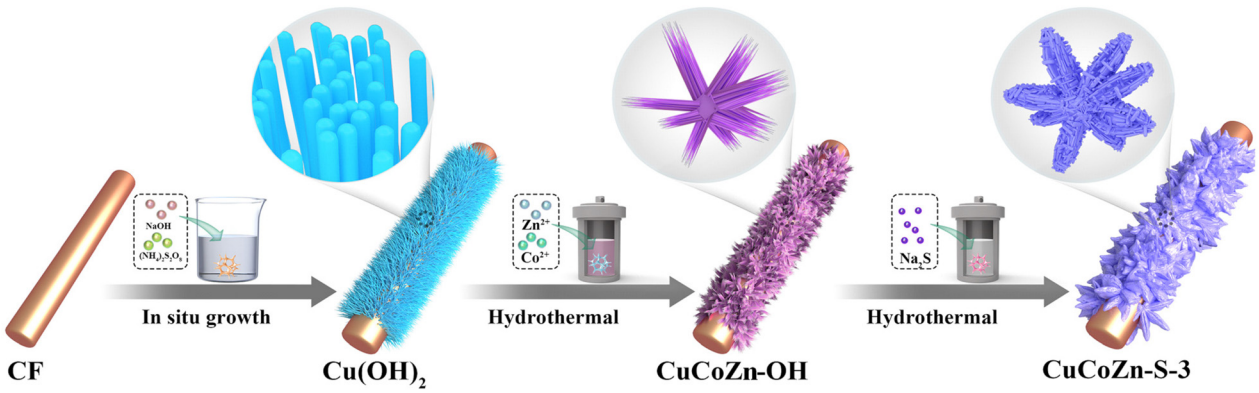

Fig. 1 Schematic diagram of the CuCoZn–S nanoflower catalyst supported on CF.

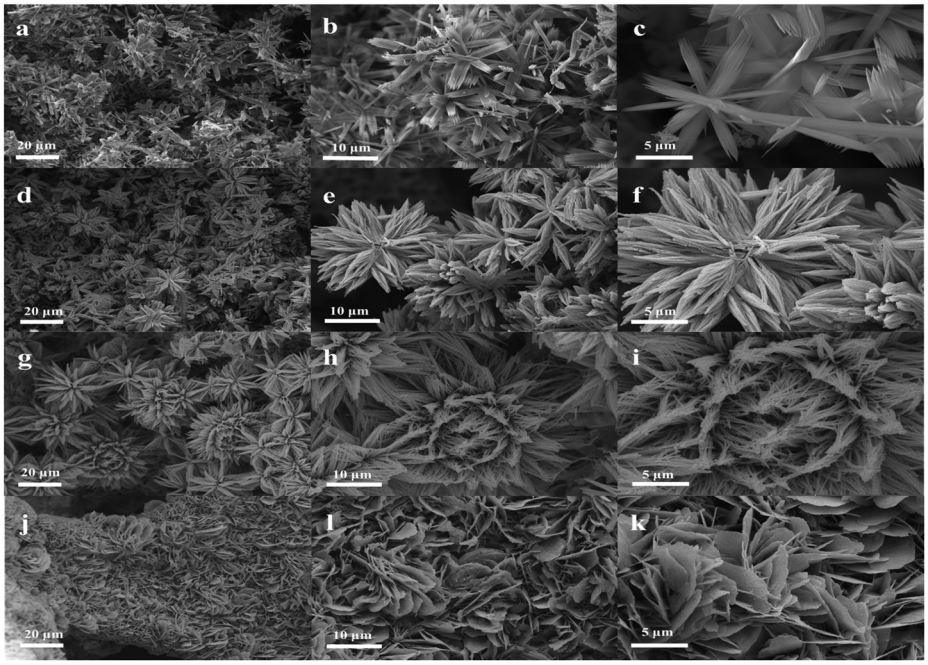

Fig. 2 SEM images of as-synthesized (a–c) CuCoZn–OH, (d–f) CuCoZn–S-3, (g–i) CuCo-S and (j and k) CuZn-S.

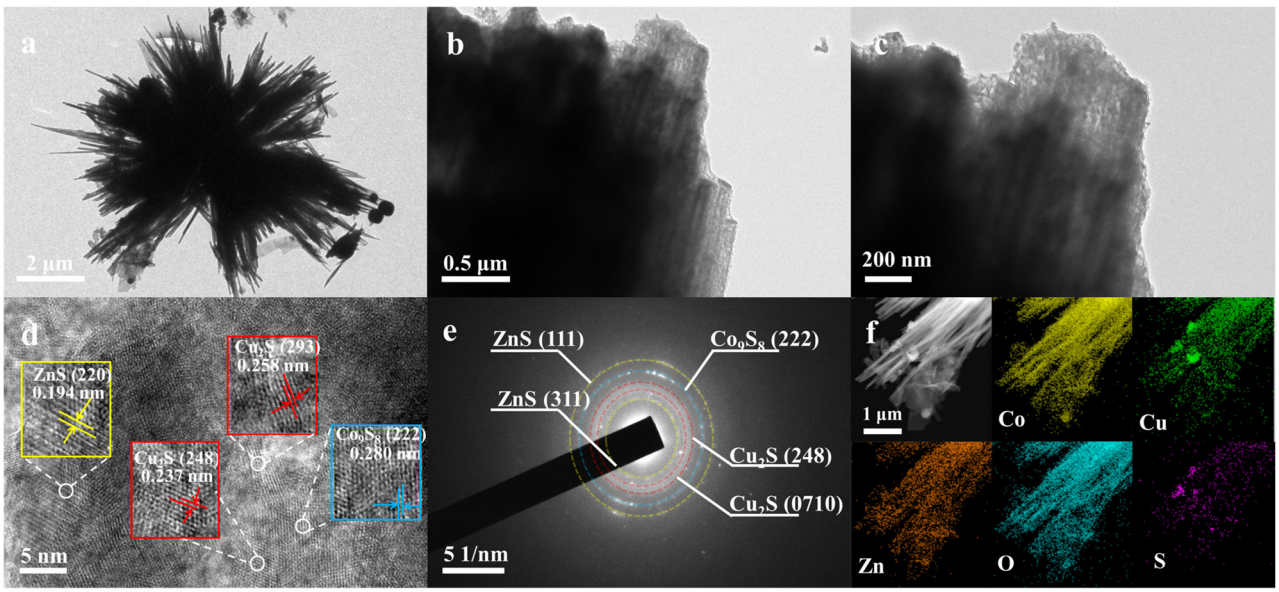

Fig. 3 (a–c) TEM images of CuCoZn–S-3 at different magnifications. (d) HRTEM images of CuCoZn–S-3. (e) SAED image. (f) EDS elemental mapping of CuCoZn–S-3.

crystal planes of Co_9S_8 correspond to a plane spacing of 0.280 nm. Moreover, the 0.194 nm spacing of ZnS is related to the (2 2 0) plane. In the selected area electron diffraction (SAED) pattern of CuCoZn–S-3 shown in Fig. 3e, the bright rings are composed of discrete speckles and fit well with the (1 1 1) and (3 1 1) crystal faces of ZnS, the (2 2 2) crystal faces of Co_9S_8, and the (2 4 8) and (0 7 10) crystal faces of Cu_2S. The EDX elemental mapping (Fig. 3f) result clearly indicates the uniform distribution of Co, Zn, Cu, O and S elements on the nanoflower structure, which clearly proved the successful formation of the CuCoZn–S-3 catalyst. Repeated inductively coupled plasma-optical emission spectrometry (ICP-OES) was performed to assess the content of Cu, Co and Zn in the catalyst CuCoZn–S-3, as listed in Table S1.†

The phase composition and crystal structure of the samples were analyzed by XRD. Fig. 4a presents the XRD patterns of

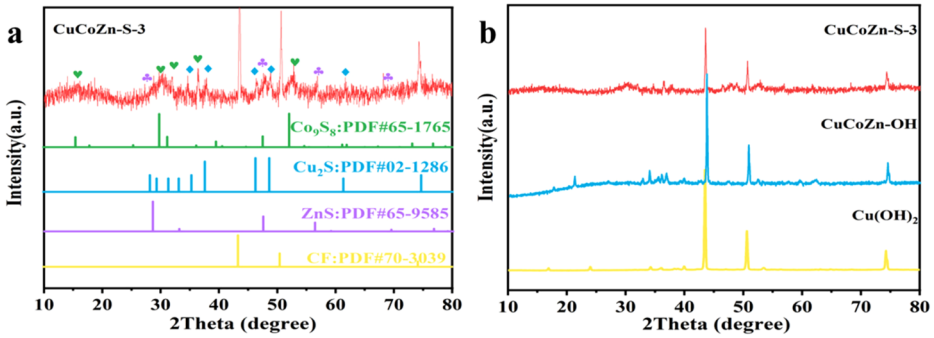

Fig. 4 (a) XRD pattern of CuCoZn–S-3. (b) XRD comparison diagram.

CuCoZn–S-3, and we can see that the three most obvious peaks located at 43.3°, 50.5° and 74.2° are indexed to the (1 1 1), (2 0 0) and (2 2 0) planes of porous CF (PDF# 70-3039), strong diffraction peaks at 2θ angles of 15.4°, 29.8°, 31.2°, 52.1° can be indexed to the (1 1 1), (3 1 1), (2 2 2) and (4 4 0) planes of Co_9S_8 (PDF# 65-1765), and Cu_2S (PDF# 02-1286) shows typical diffraction peaks centered at 35.3°, 37.6°, 46.3°, and 48.6°, corresponding to the (2 9 3), (2 4 8), (0 7 10), and (4 11 2) planes, respectively. In addition, the diffraction peaks at about 28.6°,47.5° and 56.4° are assigned to the (1 1 1), (2 2 0), and (3 1 1) facets of ZnS (PDF# 65-9585).

To disclose the electronic states and compositions of CuCoZn–S-3, X-ray photoelectron spectroscopy (XPS) spectra and comparison with the precursor CuCoZn–OH were studied. The full survey spectrum of the CuCoZn–S-3 catalyst shows the certain existence of Zn, Cu, Co, O, and S (Fig. 5a). The two main peaks at 162.6 and 161.4 eV can be grouped into the S 2p spectrum (Fig. 5b), and are labeled as $2p_{3/2}$ and $2p_{1/2}$, respectively. The reason for the low coordination of S^{2-} on the catalyst surface may be ascribed to the formation of surface sulfur defects in nanostructures. The peak at 164.3 eV corresponds to representative S–M bonds.[38] The O 1s spectrum in Fig. 5c shows that oxygen is present in three forms namely M–OH at 530.8 eV (M: Cu, Co, or Zn), oxygen vacancy at 531.7 eV and H_2O adsorption at 533.0 eV.[39–41]

Fig. 5d shows the Co 2p spectra of the CuCoZn–S-3 catalysts. Co^{2+} can be inversely convolved into $2p_{3/2}$ and $2p_{1/2}$, located at 781.7 and 797.9 eV, respectively. The peaks located at 780.0 and 795.3 eV belong to $2p_{3/2}$ and $2p_{1/2}$ of Co^{3+}. The peaks at 787.5 and 804.2 eV are satellite peaks. Compared with

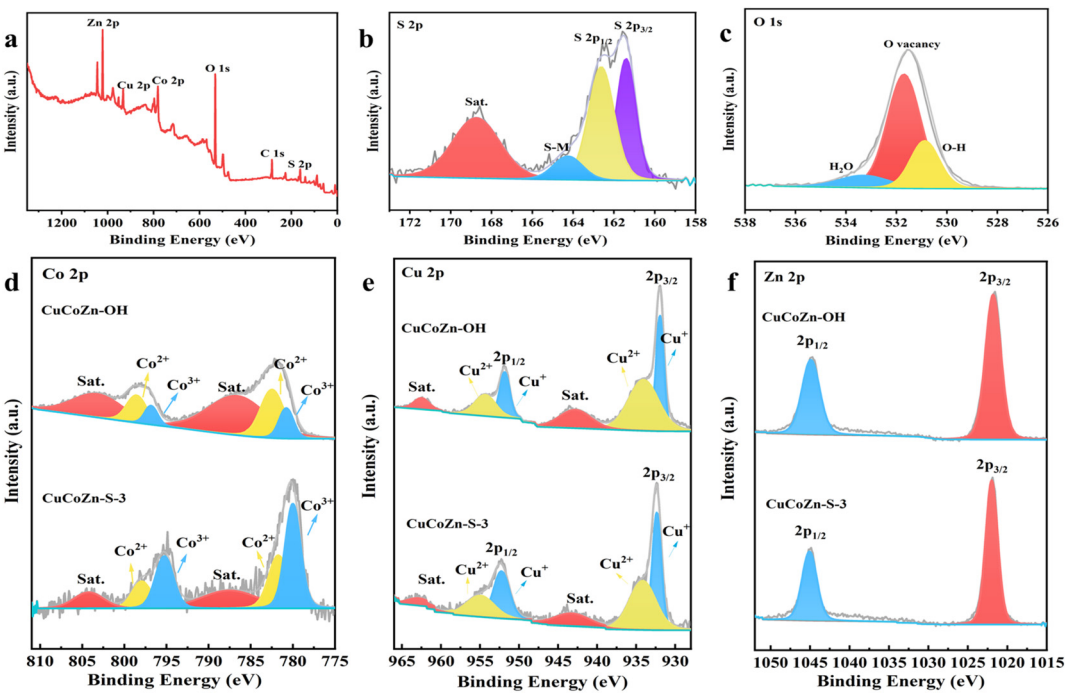

Fig. 5 (a) XPS survey spectrum of CuCoZn–S-3 and the XPS spectra of (b) S 2p, (c) O 1s, and (d) Co 2p for CuCoZn–OH and CuCoZn–S-3, (e) Cu 2p for CuCoZn–OH and CuCoZn–S-3 and (f) Zn 2p for CuCoZn–OH and CuCoZn–S-3.

CuCoZn–OH, CuCoZn–S-3 of Co $2p_{3/2}$ at 780.0 eV shifts by 0.8 eV toward a lower binding energy. This result indicates that the electronic structure of Co changes to accept the presence of electrons.[42–44]

In the Cu 2p spectrum of CuCoZn–S-3 in Fig. 5e, peaks around 952.3 eV and 932.4 eV can be assigned to Cu^{+} of $2p_{1/2}$ and $2p_{3/2}$, respectively. The peaks at 954.9 and 934.2 eV correspond to the Cu^{2+} of $2p_{1/2}$ and $2p_{3/2}$. Moreover, the peaks at 943.3 eV and 962.8 eV are satellite peaks. Compared with CuCoZn–OH of Cu $2p_{3/2}$, CuCoZn–S-3 exhibits a positively shift of 0.6 eV at 954.9 eV.[45,46] The characteristic peaks of 1020.0 and 1045.1 eV in the Zn 2p spectrum (Fig. 5f) correspond to Zn $2p_{3/2}$ and $2p_{1/2}$. Compared to CuCoZn–OH, the binding energy of the Zn $2p_{3/2}$ peak (1022.0 eV) in CuCoZn–S-3 positively shifts by 0.2 eV.[47] This further indicates that there may be electron transfer between Cu, Zn and Co, with Cu and Zn providing electrons to Co and increasing the electron density at the active site, which would be beneficial for oxygen involved electrocatalysis.[48] In summary, the synergistic effect of trimetallic ions could tailor the electronic structure and will be beneficial for redox reactions.

The electrochemical properties of the synthesized samples were determined by linear sweep voltammetry (LSV). As shown in Fig. 6a and b, the CuCoZn–S-3 catalyst displayed the best electrocatalytic activity. It requires an overpotential of only 175 mV to reach a current density of nearly 10 mA cm^{-2}, which is less than 226, 322, 432 and 236 mV of CuCoZn–OH, $Cu(OH)_2$, CF, and Ir/C, respectively. It is necessary to mention that a high current density of 100 mA cm^{-2} is achieved, and the CuCoZn–S-3 catalyst also possesses a lowest overpotential of 242 mV, while overpotentials of 307, 446, 534 and 322 mV are achieved for the CuCoZn–OH, $Cu(OH)_2$, CF, and Ir/C catalysts, respectively, which means that the sulfurization treatment exerts a significant electrocatalytic effect on the OER, and thus results in the formation of ordered nanostructures and an increase of active sites on rough surfaces. In addition, the OER performance of CuCo-S and CuZn-S was tested. As shown in Fig. S3,† CuCoZn–S-3 showed the best performance, indicating that the interaction between three metals was stronger than that between two metals. Tables S2 and S3† show a comparison of the OER performance of CuCoZn–S-3 catalysts with those of other trimetallic catalysts reported in the literature, and show that the prepared catalyst is equipped with favorable OER performance.

The Tafel slope was acquired by the conversion of the polarization curve and can be expressed using the formula: $\eta = a + b \log j$; it was positively relevant to the reaction rate of electrocatalysis, revealing the reaction kinetics of the catalyst, and thus further illustrating the OER performance of the catalyst. As shown in Fig. 6c, the CuCoZn–S-3 electrode displays a small Tafel slope of 62.3 mV dec^{-1} for the test catalysts, which is lower than those of CuCoZn–OH (82.0 mV dec^{-1}), $Cu(OH)_2$ (90.6 mV dec^{-1}), CF (110.0 mV dec^{-1}), and Ir/C (88.6 mV dec^{-1}); these results indicate that CuCoZn–S-3 is equipped with the fastest kinetics and inherent excellent OER activity.

Meanwhile, electrochemical impedance spectroscopy (EIS) reflects the charge transfer rate of the catalyst. The smaller the semicircle diameter of the Nyquist curve, the faster the charge transfer rate. In Fig. 6d, CuCoZn–S-3 exhibits lower charge transfer resistance in comparison with CuCoZn–OH, $Cu(OH)_2$, CF and Ir/C, which indicates that the unique flower-like struc-

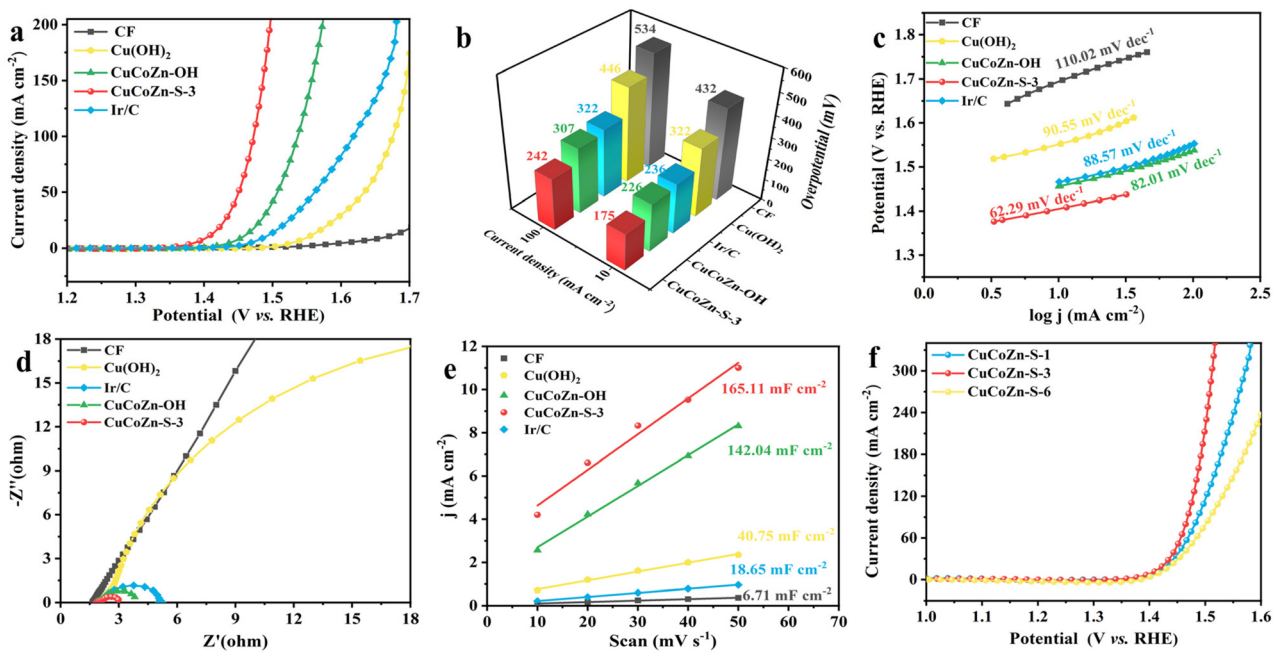

Fig. 6 OER performance test of electrocatalysts under alkaline conditions. (a) LSV polarization curves, (b) overpotential at 10 and 100 mA cm^{-2}, (c) corresponding Tafel plots, and (d) Nyquist plots. (e) C_{dl} values and (f) LSV polarization curves at different times.

ture of CuCoZn–S-3 may accelerate electron transport and catalytic dynamics.

ECSA is the electrochemically active surface area, which is closely correlated with the electrochemical double-layer capacitance C_{dl}, and it can be used to reveal the electrode reaction kinetics and interfacial reaction. C_{dl} values can be obtained by analyzing and processing CV curves, which are tested by cyclic voltammetry and obtained at scanning rates of 10, 20, 30, 40 and 50 mV S^{-1} (Fig. S4†). As displayed in Fig. 6e, the C_{dl} value of 165.1 mF cm^{-2} for CuCoZn–S-3 is larger than those of CuCoZn–OH (142.0 mF cm^{-2}), $Cu(OH)_2$ (40.8 mF cm^{-2}), CF (6.7 mF cm^{-2}) and Ir/C (18.7 mF cm^{-2}). The highest C_{dl} value of CuCoZn–S-3 manifests the most effective OER activity of the prepared catalyst. All these experimental results demonstrate that CuCoZn–S-3 contains more accelerating active sites on the surface for the OER after vulcanization, and sample electrocatalytic performance is improved. In addition, in order to study the intrinsic activity of the active sites of different samples, the ECSA was used to normalize LSV, and the formula was: ECSA normalized current density = current density × C_s/C_{dl}.[49] C_s is the specific capacitance, which can be set as 0.06 mF cm^{-2} according to the literature.[50] From Fig. S5,† we can find that the normalized LSVs still maintain the same trend as before, indicating that the active site of CuCoZn–S-3 possesses the strongest OER activity compared with those of CuCoZn–OH, $Cu(OH)_2$, and CF catalysts.

In addition, the effect of the vulcanization time (1 h, 3 h, 6 h) on the catalyst performance was also studied. Compared with CuCoZn–S-1 and CuCoZn–S-6, CuCoZn–S-3 (Table S4†) displayed the best OER performance (Fig. 6f), meanwhile possessed the smallest EIS (Fig. S6a†) and the largest C_{dl} value (Fig. S6b†). Fig. S6c and d† show the CV curves of CuCoZn–S-1 and CuCoZn–S-6. The superior performance of CuCoZn–S-3 may be due to the 3 h reaction process, which enables the catalyst to form a large degree of nano-flower structure, thus providing more electrochemical active region area, and exposing enough active sites for the subsequent reaction. During the 1 h vulcanization process, the catalyst reaction is not complete, fewer catalytic active sites are provided and catalytic performance is low. After curing for 6 h, the morphology of the catalyst changes, which results in less specific surface area, and active sites are also reduced, thus reducing the catalytic performance.

The electrocatalytic stability of CuCoZn–S-3 to the OER was assessed by continuous chronopotentiometry at a current density of 10 mA cm^{-2}. After continuous testing for 20 h as shown in Fig. 7a, the potential value was essentially unchanged. The polarization curve is pretty consistent with the initial polarization curve after the stability test (Fig. 7b). At the same time, the multistep chronopotentiometry curve of CuCoZn–S-3 was observed, by et increasing the current density by 10 mA per cm^2 per 1000 s, until it reached 100 mA cm^{-2}. When the current density changed, the potential of CuCoZn–S-3 rapidly reached a new value and leveled off (Fig. 7c). This means that CuCoZn–S-3 shows remarkable electrochemical stability. Moreover, the SEM image shows that the morphology of CuCoZn–S-3 is maintained (Fig. S7†), and it indicates the stable structure of CuCoZn–S-3. On that basis, the XPS spectrum of CuCoZn–S-3 for OER stability was further studied. By comparing the XPS before and after the stability test, it was found that the peaks of Cu, Co, Zn, O and S have changed. The high-resolution spectra (Fig. 7d–f) of Cu 2p and Zn 2p show a

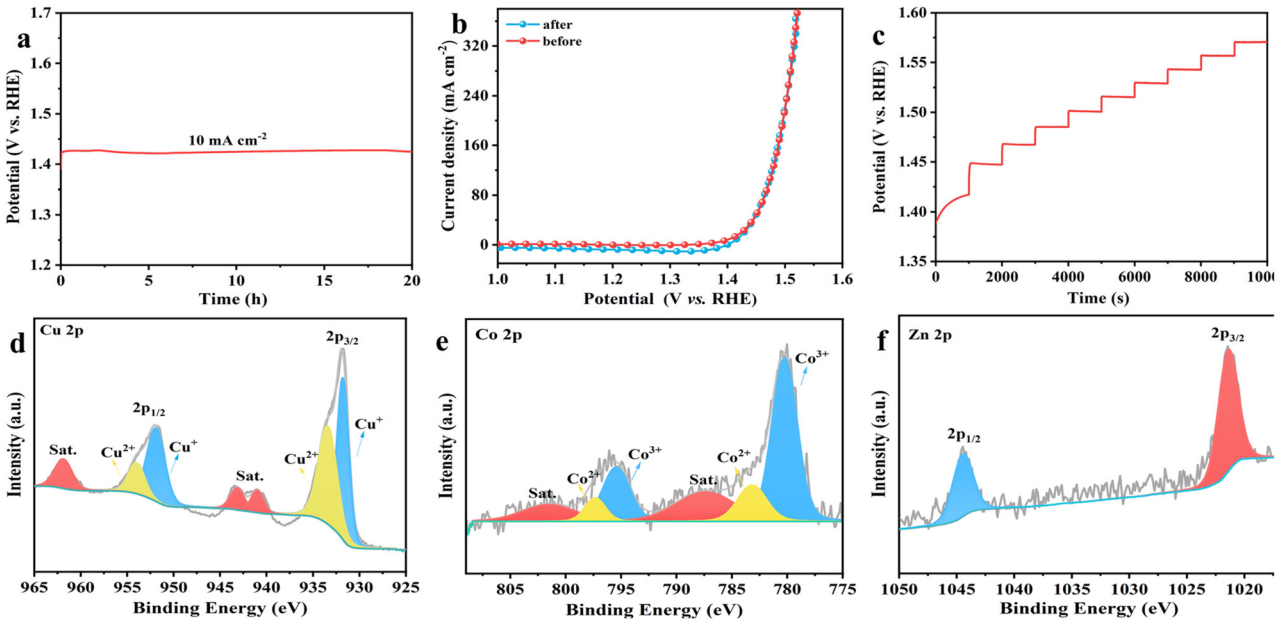

Fig. 7 (a) Stability test at a current density of 10 mA cm^{-2} for 20 h. (b) Comparison of the LSV polarization curves before and after the stability test. (c) Multi-current process curves at current densities from 10 mA cm^{-2} to 100 mA cm^{-2}. (d–f) XPS comparison spectra of Cu 2p, Co 2p and Zn 2p after the OER stability test.

similar change, shifting towards a lower binding energy, and a change in the peaks of Cu $2p_{3/2}$ at 933.4 eV occurs with a negative shift of 0.6 eV; the ratio of Cu^{+}/Cu^{2+} increased from 0.82 to 1.02.[51] The peak of Zn 2p is obviously weakened and its content decreases. Co $2p_{3/2}$ has a positive shift of 0.8 eV at 780.0 eV, and the content ratio of Co^{2+}/Co^{3+} calculated from fitting peak areas is decreased from 0.63 to 0.26; this indicates that the formation of Co^{3+} and Co^{3+} may replace the positions of Cu^{2+} and Zn^{2+}, becoming the main activity centers of the reaction.[52,53] In the S 2p of the M–S peak is weaker, indicating that the sulfides have been oxidized, possibly to form an oxide or hydroxide. At the same time, the peak of S 2p (Fig. S8a†) at 162.2 eV becomes weaker, indicating that S^{2-} is leached out and may be replaced by oxygen.[54] The M–O peak appears at 529.7 eV in O 1s (Fig. S8b†), and the peak of M–OH becomes larger.[55] These results suggest metal oxy-hydroxides as the actual reaction site's major activity centers and that the existence of sulfide will improve the activity.[56,57]

4. Conclusions

In summary, a unique nanoflower-like CuCoZn–S-3 catalyst was synthesized by one-step pretreatment by growing $Cu(OH)_2$ on CF and replacing Cu ions in the substrate. The nanoflower-like structure enables the catalyst to display enough electroactive area, fully contact the electrolyte, and enhance ion diffusion and electron transport. The polymetallic and sulfide compositions make the materials rich in redox reactions, enable strong synergies and result in remarkable electrical conductivity. Due to its unique structure and composition, CuCoZn–S-3 exhibits excellent OER electrocatalytic performance in basic solution (1 M KOH). When overpotentials of CuCoZn–S-3 reach 175 mV and 242 mV, the corresponding current densities are 10 mA cm^{-2} and 100 mA cm^{-2}, with a Tafel slope of 62.3 mV, respectively. In a 20 h stability test, the overpotential remained relatively stable, and the structure of the catalyst was basically unchanged. This strategy for constructing highly efficient alkaline OER electrocatalysts with polymetals may be worthy of wider application with other non-precious metals.

Author contributions

Jie Bai: conceptualization, methodology, validation, data curation, and writing – original draft. Nana Lei: methodology and validation. Limin Wang: methodology, validation and supervision. Yaqiong Gong: conceptualization, supervision, project administration, funding acquisition, and writing – review & editing.

Conflicts of interest

The authors declare that they have no known competing financial interests or personal relationships that could have appeared to influence the work reported in this paper.

Acknowledgements

This work was financially supported by the National Natural Science Foundation of China (22271262) and the Shanxi Scholarship Council of China (2019070).

References

1 M. S. Dresselhaus and I. L. Thomas, *Nature*, 2001, **414**, 332–337.
2 S. Chu and A. Majumdar, *Nature*, 2012, **488**, 294–303.
3 J. A. Turner, *Science*, 2004, **305**, 972–974.
4 W. Jiang, T. Tang, Y. Zhang and J. Hu, *Acc. Chem. Res.*, 2020, **53**, 1111–1123.
5 F. Yu, L. Yu, I. K. Mishra, Y. Yu, Z. Ren and H. Zhou, *Mater. Today Phys.*, 2018, **7**, 121–138.
6 E. Fabbri and T. J. Schmidt, *ACS Catal.*, 2018, **8**, 9765–9774.
7 Y. Pi, N. Zhang, S. Guo, J. Guo and X. Huang, *Nano Lett.*, 2016, **16**, 4424–4430.
8 T. Reier, M. Oezaslan and P. Strasser, *ACS Catal.*, 2012, **2**, 1765–1772.
9 H. Osgood, S. V. Devaguptapu, H. Xu, J. Cho and G. Wu, *Nano Today*, 2016, **11**, 601–625.
10 Y. Zhu, X. Liu, S. Jin, H. Chen, W. Lee, M. Liu and Y. Chen, *J. Mater. Chem. A*, 2019, **7**, 5875–5897.
11 M. Qu, Y. Jiang, M. Yang, S. Liu, Q. Guo, W. Shen, M. Li and R. He, *Appl. Catal., B*, 2020, **263**, 118324.
12 M. Sun, H. Liu, J. Qu and J. Li, *Adv. Energy Mater.*, 2016, **6**, 1600087.
13 Y. Guo, T. Park, J. W. Yi, J. Henzie, J. Kim, Z. Wang, B. Jiang, Y. Bando, Y. Sugahara, J. Tang and Y. Yamauchi, *Adv. Mater.*, 2019, **31**, 1807134.
14 Y. Zhao, C. K. Mavrokefalos, P. Zhang, R. Erni, J. Li, C. A. Triana and G. R. Patzke, *Chem. Mater.*, 2020, **32**, 1371–1383.
15 X. Peng, C. Pi, X. Zhang, S. Li, K. Huo and P. K. Chu, *Sustainable Energy Fuels*, 2019, **3**, 366–381.
16 Y. Zhang, B. Ouyang, J. Xu, G. Jia, S. Chen, R. S. Rawat and H. J. Fan, *Angew. Chem., Int. Ed.*, 2016, **55**, 8670–8674.
17 J. Bai, T. Zhou, Y. Gao, M. Zhang, X. Jing and Y. Gong, *Dalton Trans.*, 2022, **51**, 4853–4861.
18 Y. Wang, S. Tao, H. Lin, G. Wang, K. Zhao, R. Cai, K. Tao, C. Zhang, M. Sun, J. Hu, B. Huang and S. Yang, *Nano Energy*, 2021, **81**, 105606.
19 H. Liao, G. Ni, P. Tan, Y. Liu, K. Chen, G. Wang, M. Liu and J. Pan, *Appl. Catal., B*, 2022, **317**, 121713.
20 L. L. Wu, Q. S. Wang, J. Li, Y. Long, Y. Liu, S. Y. Song and H. J. Zhang, *Small*, 2018, **14**, 1704035.
21 Y. Gan, X. Dai, M. Cui, H. Zhao, F. Nie, Z. Ren, X. Yin, Z. Yang, B. Wu, Y. Cao and X. Zhang, *J. Mater. Chem. A*, 2021, **9**, 9858–9863.
22 Y. Yan, B. Y. Xia, B. Zhao and X. Wang, *J. Mater. Chem. A*, 2016, **4**, 17587–17603.
23 N. Manivelan, S. Karuppanan and K. Prabakar, *ACS Appl. Mater. Interfaces*, 2022, **14**, 30812–30823.

24 R. Zhang, L. Cheng, Z. Wang, F. Kong, Y. Tsegazab, W. Lv and W. Wang, *Appl. Surf. Sci.*, 2020, **526**, 146753.
25 D. Chinnadurai, R. Rajendiran and P. Kandasamy, *J. Colloid Interface Sci.*, 2022, **606**, 101–112.
26 B. Wang, Y. Chen, X. Wang, J. Ramkumar, X. Zhang, B. Yu, D. Yang, M. Karpuraranjith and W. Zhang, *J. Mater. Chem. A*, 2020, **8**, 13558–13571.
27 Z. Huang, J. Wang, Y. Peng, C. Jung, A. Fisher and X. Wang, *Adv. Energy Mater.*, 2017, **7**, 1700544.
28 Z. Chen, X. Liao, C. Sun, K. Zhao, D. Ye, J. Li, G. Wu, J. Fang, H. Zhao and J. Zhang, *Appl. Catal., B*, 2021, **288**, 120021.
29 L. Zhuang, Y. Jia, H. Liu, X. Wang, R. K. Hocking, H. Liu, J. Chen, L. Ge, L. Zhang, M. Li, C. L. Dong, Y. C. Huang, S. Shen, D. Yang, Z. Zhu and X. Yao, *Adv. Mater.*, 2019, **31**, 1805581.
30 Q. Huang, B. Wang, S. Ye, H. Liu, H. Chi, X. Liu, H. Fan, M. Li, C. Ding, Z. Li and C. Li, *ACS Catal.*, 2021, **12**, 491–496.
31 M. Ahmad, I. Hussain, T. Nawaz, Y. Li, X. Chen, S. Ali, M. Imran, X. Ma and K. Zhang, *J. Power Sources*, 2022, **534**, 231414.
32 W. Luo, X. Cao, S. Liang, J. Huang, Q. Su, Y. Wang, G. Fang, L. Shan and J. Zhou, *ACS Appl. Energy Mater.*, 2019, **2**, 4567–4575.
33 H. Yang, B. Wang, H. Li, B. Ni, K. Wang, Q. Zhang and X. Wang, *Adv. Energy Mater.*, 2018, **8**, 1801839.
34 K. Xiao, J. Wei, W. Han and Z. Liu, *J. Power Sources*, 2021, **487**, 229408.
35 Z. Yin, R. He, Y. Zhang, L. Feng, X. Wu, T. Wågberg and G. Hu, *J. Energy Chem.*, 2022, **69**, 585–592.
36 S. Wang, L. Zhao, J. Li, X. Tian, X. Wu and L. Feng, *J. Energy Chem.*, 2022, **66**, 483–492.
37 M. Ning, L. Wu, F. Zhang, D. Wang, S. Song, T. Tong, J. Bao, S. Chen, L. Yu and Z. Ren, *Mater. Today Phys.*, 2021, **19**, 100419.
38 W. Li, L. Wu, X. Wu, C. Shi, Y. Li, L. Zhang, H. Mi, Q. Zhang, C. He and X. Ren, *Appl. Catal., B*, 2022, **303**, 120849.
39 X. Yu, W. Zhang, L. She, Y. Zhu, Y. Fautrelle, Z. Ren, G. Cao, X. Lu and X. Li, *Chem. Eng. J.*, 2022, **430**, 133073.
40 X. Du, J. Guo, M. Chen, W. C. Cheng, Y. Chen, D. Liu, S. Chen, X. Wang, K. H. Lo, J. Hu and H. Pan, *Chem. Eng. J.*, 2021, **425**, 131662.
41 H. R. Devi, R. Chikkegowda, D. Rangappa, A. K. Yadav, Z. Chen and K. K. Nanda, *Chem. Eng. J.*, 2022, **435**, 135019.
42 M. Li, J. Wang, F. Wang, Y. Zhai, X. Zhang, H. Lv, T. Yu and G. Lv, *Appl. Surf. Sci.*, 2021, **568**, 150900.
43 S. Zhang, D. Zhai, T. Sun, A. Han, Y. Zhai, W. C. Cheong, Y. Liu, C. Su, D. Wang and Y. Li, *Appl. Catal., B*, 2019, **254**, 186–193.
44 Y. Yang, H. Yao, Z. Yu, S. M. Islam, H. He, M. Yuan, Y. Yue, K. Xu, W. Hao, G. Sun, H. Li, S. Ma, P. Zapol and M. G. Kanatzidis, *J. Am. Chem. Soc.*, 2019, **141**, 10417–10430.
45 Z. Zang, X. Wang, X. Li, Q. Zhao, L. Li, X. Yang, X. Yu, X. Zhang and Z. Lu, *ACS Appl. Mater. Interfaces*, 2021, **13**, 9865–9874.
46 S. Zhang, Y. Sun, F. Liao, Y. Shen, H. Shi and M. Shao, *Electrochim. Acta*, 2018, **283**, 1695–1701.
47 C. Zhang, R. Lu, C. Liu, J. Lu, Y. Zou, L. Yuan, J. Wang, G. Wang, Y. Zhao and C. Yu, *Adv. Sci.*, 2022, **9**, 2104768.
48 Y. Li, W. Hua, Y. Guo, S. Liang, B. Li, L. Wang and J. G. Wang, *J. Colloid Interface Sci.*, 2022, **617**, 391–398.
49 M. Zhang, Y. Zhang, L. Ye, B. Guo and Y. Gong, *Appl. Catal., B*, 2021, **298**, 120601.
50 F. Zhou, R. Sa, X. Zhang, S. Zhang, Z. Wen and R. Wang, *Appl. Catal., B*, 2020, **274**, 119092.
51 G. Zhang, R. Zhu, R. Zhang, D. Zhang, C. Sun, Z. Long and Y. Li, *J. Power Sources*, 2022, **523**, 231031.
52 Y. Zhang, L. Ye, M. Zhang, L. Ma and Y. Gong, *Appl. Surf. Sci.*, 2022, **589**, 152957.
53 C. Wang, M. Zhu, Z. Cao, P. Zhu, Y. Cao, X. Xu, C. Xu and Z. Yin, *Appl. Catal., B*, 2021, **291**, 120071.
54 P. Yang, F. Kong, X. Sui, L. Zhao, Y. Qiu, H. Zhang and Z. Wang, *Int. J. Hydrogen Energy*, 2022, **47**, 8811–8819.
55 Z. Han, G. Li, X. Zeng, Y. Zhu, N. Li, J. Zhang, W. Zhao and Q. Jiao, *Int. J. Hydrogen Energy*, 2022, **47**, 15695–15705.
56 H. Li, S. Yang, W. Wei, M. Zhang, Z. Jiang, Z. Yan and J. Xie, *J. Colloid Interface Sci.*, 2022, **608**, 536–548.
57 T. Zhou, J. Bai, Y. Gao, L. Zhao, X. Jing and Y. Gong, *J. Colloid Interface Sci.*, 2022, **615**, 256–264.